



OPEN

# Optimizing microfluidic chip for rapid SARS-CoV-2 detection using Taguchi method and artificial neural network PSO

Sameh Kaziz<sup>1</sup>, Fraj Echouchene<sup>2,3</sup> & Mohamed Hichem Gazzah<sup>4</sup>✉

Microfluidic biosensors offer a promising solution for real-time analysis of coronaviruses with minimal sample volumes. This study optimizes a biochip for the rapid detection of SARS-CoV-2 using the Taguchi orthogonal table  $L_9(3^4)$ , which comprises nine groups of experiments varying four key parameters: Reynolds number (Re), Damköhler number (Da), Schmidt number (Sc), and the dimensionless position of the reaction surface (X). Signal-to-noise (S/N) ratios and analysis of variance (ANOVA) are employed to determine optimal parameters and assess their impact on binding kinetics and response time of the detection device. These obtained optimal parameters correspond to  $Re = 4 \cdot 10^2$ ,  $Da = 1000$ ,  $Sc = 10^5$ , and  $X = 1$ . Additionally, results highlight Da as the most influential factor, accounting for 91%, while X has a minimal effect of 0.3%. Furthermore, an artificial neural network optimization technique, specifically particle swarm optimization (PSO), was utilized to predict biosensor performance. Derived from the Full  $L_{81}(3^4)$  design experiment, the PSO model demonstrates its effectiveness compared to the conventional multi-layer perception (MLP) model, thus underlining its potential in this innovative optimization context.

**Keywords** ANOVA, Biosensor, SARS-CoV-2, Particle swarm optimization, Taguchi method

Early detection of COVID-19 is crucial for effective pandemic management, enabling rapid isolation, preventing disease spread, and facilitating early treatment. The primary method for detecting SARS-CoV-2 is real-time reverse transcription polymerase chain reaction (RT-PCR)<sup>1,2</sup>. However, RT-PCR diagnostics require expensive reagents, specialized equipment, and trained personnel<sup>3</sup>. While conventional RT-PCR is often time-consuming, recent advancements in microfluidic-based PCR have significantly improved speed, cost-effectiveness, and sensitivity<sup>4</sup>. These techniques offer rapid amplification, reduced reagent consumption, and lower detection limits, making them competitive with traditional methods<sup>5</sup>.

To further reduce detection time, various point-of-care (POC) biosensors have been developed<sup>1,6–8</sup>, targeting antigens, antibodies, or nucleic acids<sup>7</sup>. While antibody tests are suitable for late-stage infections, nucleic acid-based detection methods are preferred for early-stage diagnosis due to their superior sensitivity and specificity. However, nucleic acid testing involves more complex processes such as extraction, amplification, and detection<sup>9</sup>. Although RT-PCR remains clinically more sensitive and specific than POC biosensors, immunodiagnostic assays offer a reliable and cost-effective alternative by improving specific immunoassays for desired antigen proteins.

Immunoassays, based on antigen-antibody interactions, have garnered significant interest in fields such as medicine and environmental monitoring<sup>10</sup>. Traditional immunoassays include complex detection protocols and require skilled professionals. Moreover, diffusion-limited reaction kinetics and lengthy incubation steps limit their broad applications<sup>11</sup>. To address unmet medical needs like early and rapid disease diagnosis, immunoassays are increasingly being adapted to microfluidic formats<sup>12</sup>. This miniaturization technology enhances analysis performance by integrating multiple processes into a single chip, reducing analysis time and increasing sensitivity and reliability with minimal reagent use<sup>13</sup>. Microfluidic chip technology allows for the simultaneous detection of different samples, which is valuable in protein chips. However, its use is limited

<sup>1</sup>NANOMISENE Laboratory, LR16CRMN01, Centre for Research on Microelectronics and Nanotechnology (CRMN) of Sousse Technopole, Sousse, Tunisia. <sup>2</sup>Higher Institute of Applied Sciences and Technology of Sousse, University of Sousse, Ettafala City, Ibn Khaldoun, Sousse 4003, Tunisia. <sup>3</sup>Laboratory of Electronics and Microelectronics LR99ES30, Faculty of Sciences, University of Monastir, Monastir 5000, Tunisia. <sup>4</sup>Quantum and Statistical Physics Laboratory, Faculty of Sciences of Monastir, University of Monastir, Environment Boulevard, Monastir 5019, Tunisia. ✉email: hichem.gazzah@fsm.rnu.tn

by the diffusion transport of antigens in laminar flow, where low antigen concentrations delay detection<sup>14</sup>. To improve the sensitivity of microfluidic chips, many numerical and experimental studies have been conducted. Various physical mechanisms, such as magnetic effects<sup>15</sup>, optical forces<sup>16</sup>, and electrokinetic effects<sup>17–19</sup>, have been applied to enhance flow agitation and biosensor binding reaction rates. Other studies<sup>19,20</sup> have analyzed the effects of reaction surface and electrodes shapes on biosensor performance. Shahbazi et al.<sup>21</sup> demonstrated that the reaction surface's location relative to the channel inlet significantly impacts microfluidic biosensor efficiency.

In related fields, recent studies have explored novel techniques for rapid and sensitive detection of various analytes, underscoring the necessity for continuous development in this area<sup>22–24</sup>. Among these advancements, the use of nanomaterials in biosensing has shown great potential in various applications. Nanomaterial-based electrochemical biosensing has been effectively employed to detect fumonisins, demonstrating the importance of developing sensitive detection techniques<sup>25</sup>. Furthermore, the use of metal-organic frameworks (MOFs) for electrochemical-based sensing platforms has shown promising results in detecting glucose and hydrogen peroxide<sup>26</sup>. These advancements illustrate the broader applicability and importance of developing specialized assays for different analytes.

Other research has identified several factors influencing the kinetics of antigen-antibody binding reactions in microfluidic biosensors, including flow velocity, target antigen concentration, reaction surface position, microfluidic dimensions, and biosensor shape. Optimizing these factors is crucial for enhancing immunoassay performance. Taguchi's experimental design is a well-known technique for process optimization, providing a systematic and efficient methodology<sup>27–29</sup>. Taguchi's method aims to design quality into the product by optimizing control factors through simple tools like signal-to-noise ratio (S/N) and analysis of variance (ANOVA)<sup>28</sup>.

Additionally, integrating artificial intelligence (AI) and machine learning has become prominent in optimizing microfluidic biosensor performance. Machine learning algorithms address complex and nonlinear problems, aiding in rapid and accurate data analysis and optimization. Specifically, Particle Swarm Optimization (PSO) combined with Artificial Neural Networks (ANN-PSO) has been applied to enhance detection device performance<sup>30–32</sup>. ANN models assist in predictive modeling and optimization, while PSO fine-tunes ANN parameters, improving prediction accuracy and control. This approach aligns with recent advancements<sup>33–35</sup> highlighting the innovative integration of optimization techniques in engineering and biomedical applications.

To improve future sensing devices, this study aims to optimize control parameters such as Reynolds number, Damköhler number, Schmidt number, and reaction surface position to reduce the response time of a microfluidic biosensor for SARS-CoV-2 detection. The design of experiments uses Taguchi's L<sub>9</sub> orthogonal array<sup>36,37</sup>, and machine learning models, specifically ANN-PSO, are developed to predict the microfluidic chip's performance.

The originality and novelty of this work lie in using the Taguchi method combined with the PSO algorithm to predict biosensor performance for rapid SARS-CoV-2 detection. This approach offers potential advantages in efficiency, cost, and detection time. Unlike previous research focused on structural parameters<sup>17–19,21</sup>, our study prioritizes optimizing dimensionless numbers (Reynolds, Damköhler, and Schmidt numbers), providing a more comprehensive understanding and applicability across diverse microfluidic systems.

## Biochip design

Figure 1a,b illustrates the geometry of the studied microfluidic chip. The microchannel has a length (L) of 250  $\mu\text{m}$  and a height (H) of 40  $\mu\text{m}$ . The reaction surface, measuring 20  $\mu\text{m}$ , is situated on the bottom wall at a specific x position from the inlet of the microchannel. The carrier fluid, composed of water mixed with antigens (SARS-CoV-2), flows through the microchannel from left to right. Initially, ligands (antibodies) are immobilized on the reaction surface.

## Model equations

### Modeling Navier-Stokes equations

The fluid carrying antigens, assumed to be Newtonian and incompressible, flows in a laminar regime inside the microchannel. The continuity equation for incompressible fluids is:

$$\frac{\partial u}{\partial x} + \frac{\partial v}{\partial y} = 0 \quad (1)$$

Consequently, the 2D Navier-Stokes equations are employed to ascertain the fluid velocity field in the microchannel, as presented in Eqs. (2) and (3):

$$\rho \left( u \frac{\partial u}{\partial x} + v \frac{\partial u}{\partial y} \right) = - \frac{\partial p}{\partial x} + \mu \left( \frac{\partial^2 u}{\partial x^2} + \frac{\partial^2 u}{\partial y^2} \right) \quad (2)$$

$$\rho \left( u \frac{\partial v}{\partial x} + v \frac{\partial v}{\partial y} \right) = - \frac{\partial p}{\partial y} + \mu \left( \frac{\partial^2 v}{\partial x^2} + \frac{\partial^2 v}{\partial y^2} \right) \quad (3)$$

Here,  $u$  and  $v$  represent the components of the flow velocity field, while  $p$ ,  $\rho$ , and  $\mu$  denote the pressure, density, and dynamic viscosity of the fluid, respectively.

### Modeling the antigen transport equation

The diffusion-convection transport of the target antigen is modeled using Fick's second law, as shown in Eq. (4):

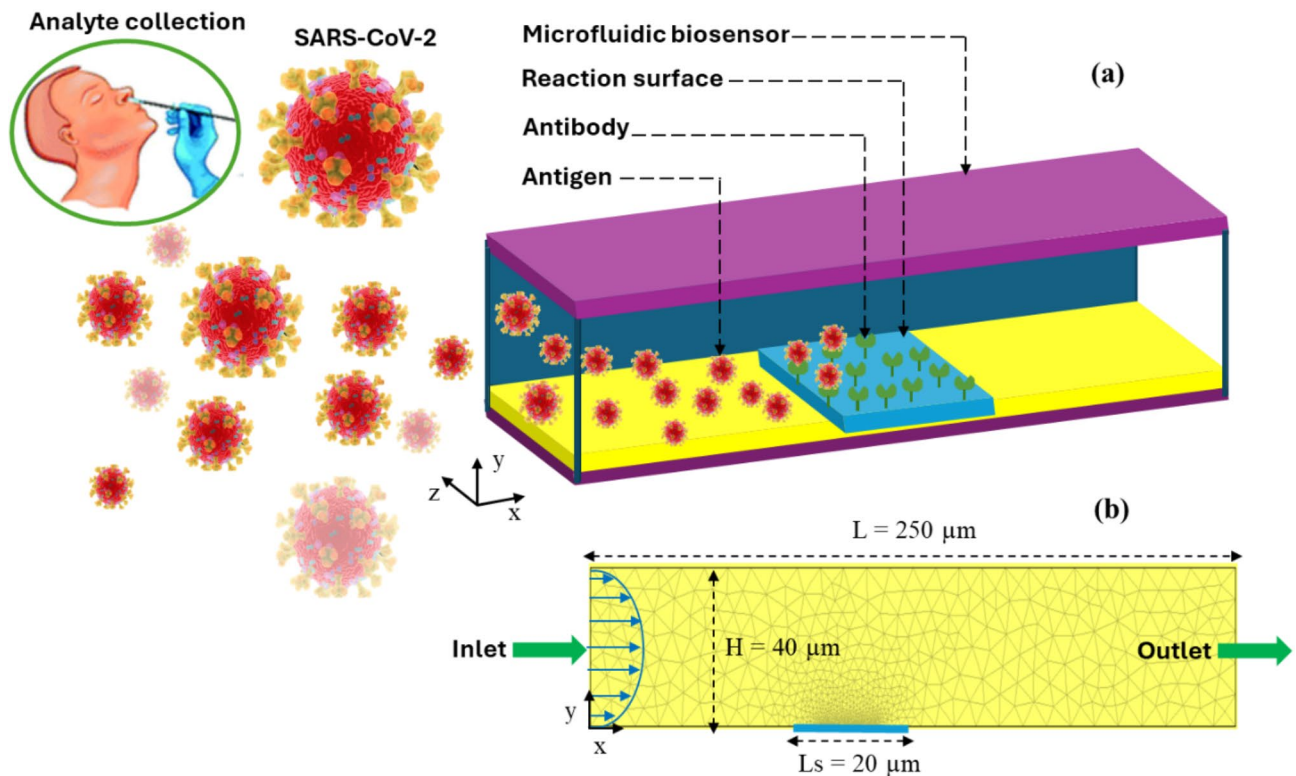


**Fig. 1.** (a) Microfluidic biochip design. (b) 2D numerical domain. The 3D representation was generated using Microsoft PowerPoint 2016.

$$\frac{\partial [A]}{\partial t} + u \frac{\partial [A]}{\partial x} + v \frac{\partial [A]}{\partial y} = D \left( \frac{\partial^2 [A]}{\partial x^2} + \frac{\partial^2 [A]}{\partial y^2} \right) \quad (4)$$

where [A] and D denote the concentration and the diffusion constant of the target antigen, respectively.

#### Modeling the binding kinetics of the antigen-antibody reaction

Antigen molecules (analytes A) are transported by diffusion and convection to reach free binding sites (ligands B) immobilized on the sensitive surface. This process results in the formation of an analyte-ligand complex (AB), as described by the following reaction:



According to the first-order Langmuir-Hinshelwood adsorption model<sup>38</sup>, the formation of the antigen-antibody complex (AB) is described by:

$$\frac{\partial [AB]}{\partial t} = k_{on} [A_{surf}] \cdot [B_{free}] - k_{off} [AB] \quad (6)$$

where [AB] represents the surface concentration of the complex, [A<sub>surf</sub>] is the volume analyte concentration at the binding surface, [B<sub>free</sub>] is the surface concentration of free ligands, k<sub>on</sub> is the complex association rate constant, and k<sub>off</sub> is the complex dissociation rate constant. The equilibrium of the reaction is described by the equilibrium dissociation constant  $K_d = \frac{k_{off}}{k_{on}}$ .

As illustrated in Fig. 2, the concentration of available binding sites on the sensitive surface [B<sub>max</sub>] is equal to the sum of the concentrations of free binding sites [B<sub>free</sub>] and the bound complexes [AB]:

$$[B_{max}] = [B_{free}] + [AB] \quad (7)$$

The Eq. (6) is then written as (Eq. (8)):

$$\frac{\partial [AB]}{\partial t} = k_{on} [A_{surf}] \cdot ([B_{max}] - [AB]) - k_{off} [AB] \quad (8)$$

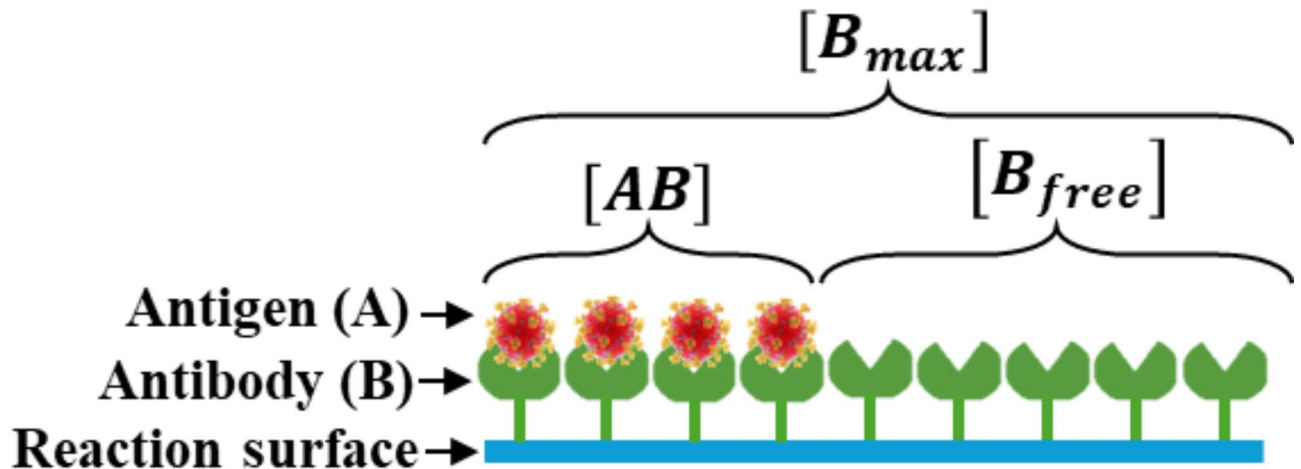


Fig. 2. Antigen-antibody kinetic reaction.

### Dimensionless model equations

The model equations have been transformed into a dimensionless form as follows: The two components of the velocity vector are scaled by  $u_0$ , which is the average velocity of the fluid at the inlet of the microchannel. The time, pressure and x and y coordinates are scaled by the diffusion transport time  $\frac{H^2}{D}$ , the pressure scale  $\rho u_0$ , and the length of the channel  $H$ , respectively. The surface concentration of the antigen-antibody complexes and the volume concentration of antigen molecules are scaled by the factors  $[B_{max}]$  and  $[A_0]$  respectively, where  $[A_0]$  is the antigen concentration at the inlet of the microchannel.

The dimensionless form of Eqs. 1, 2, 3, 4 and 8 is then written as Eqs. 9, 10, 11, 12 and 13:

$$\frac{\partial u^*}{\partial x^*} + \frac{\partial v^*}{\partial y^*} = 0 \quad (9)$$

$$u^* \frac{\partial u^*}{\partial x^*} + v^* \frac{\partial u^*}{\partial y^*} = - \frac{\partial p^*}{\partial x^*} + \frac{1}{Re} \left( \frac{\partial^2 u^*}{\partial x^{*2}} + \frac{\partial^2 u^*}{\partial y^{*2}} \right) \quad (10)$$

$$u^* \frac{\partial v^*}{\partial x^*} + v^* \frac{\partial v^*}{\partial y^*} = - \frac{\partial p^*}{\partial y^*} + \frac{1}{Re} \left( \frac{\partial^2 v^*}{\partial x^{*2}} + \frac{\partial^2 v^*}{\partial y^{*2}} \right) \quad (11)$$

$$\frac{\partial [A]^*}{\partial t^*} + Pe \left( u^* \frac{\partial [A]^*}{\partial x^*} + v^* \frac{\partial [A]^*}{\partial y^*} \right) = \frac{\partial^2 [A]^*}{\partial x^{*2}} + \frac{\partial^2 [A]^*}{\partial y^{*2}} \quad (12)$$

$$\frac{\partial [AB]^*}{\partial t^*} = Da \cdot \sigma [[A_{surf}]^* \cdot ([1 - [AB]^*]) - K_d [AB]^*] \quad (13)$$

where

$$u^* = \frac{u}{u_0}, v^* = \frac{v}{v_0}, x^* = \frac{x}{H}, y^* = \frac{y}{H}, t^* = \frac{t}{t_0}, [A]^* = \frac{[A]}{[A_0]}, t_0 = \frac{H^2}{D}, p^* = \frac{p}{p_0}, p_0 = \frac{1}{2} \rho u_0^2$$

where  $Re = \frac{\rho u_0 H}{\mu}$  represents the Reynolds number,  $Pe = \frac{u_0 H}{D}$  is the Peclet number,  $Da = \frac{K_{on} [B_{max}] H}{D}$  is the Damkohler number,  $\sigma = \frac{H [A_0]}{[B_{max}]}$  is the relative density of the analyte-ligand complex, and  $K_d = \frac{K_{off}}{K_{on} [A_0]}$  is the dimensionless equilibrium dissociation constant. The Damkohler number, used in chemical kinetics, defines the ratio between the characteristic diffusion time of the antigen (rate of the transport  $\frac{D}{H}$ ) and the characteristic reaction time for complex formation (reaction velocity  $K_{on} \cdot [B_{max}]$ ).

$Da > 1$  indicates a transport-limited system, whereas  $Da < 1$  specifies a reaction-rate-limited system. In the case of large molecules, such as the analyte in this study,  $Da$  will be large due to the small diffusion coefficient<sup>39</sup>.

The detection time of the microfluidic biosensor is a crucial parameter of the analyte-ligand chemical kinetics, representing the duration required for the concentration of the analyte-ligand complex to reach 95% of its threshold value. Here the spatially averaged dimensionless concentration of AB complexes is defined as:

$$\langle [AB] \rangle = \frac{1}{l_s} \int_0^{l_s} [AB] (x, t) dx \quad (14)$$

where  $l_s = \frac{l_s}{H}$  is the dimensionless length of the binding surface.

### Boundary and initial conditions

For the modeling of the laminar flow, at the inlet of the microfluidic channel, the fluid flows with a parabolic velocity profile of average value  $u_0$ . At the outlet, the flow is assumed to be fully developed. For the lower and upper microchannel walls, including the reaction surface, the no-slip condition is applied. Regarding the modeling of antigen transport, a constant volume concentration  $[A]_0$  and a convective flow condition,  $\vec{n} \cdot (D \nabla [A]) = 0$ , were imposed at the inlet and outlet of the microchannel, respectively. For the reaction surface, the condition of diffusive flux balanced by the temporal flow rate was applied. For the rest of the microchannel walls, they are assumed to be impermeable (i.e., they do not interact with the target antigens) and the homogeneous Neumann condition was adopted<sup>17,21</sup>.

For the initial conditions concerning Eqs. (12) and (13), the analyte and surface complex concentrations were initially set to zero:  $[A]_{(t=0)} = 0$  and  $[AB]_{(t=0)} = 0$ .

### Simulations protocols

To solve the model comprising Eqs. (9–13), the finite element method (FEM) was employed<sup>40</sup>. The 2D domain is divided into triangular cells, with mesh refinement near the sensitive surface. The numerical resolution process is shown in Fig. 3. The transport equations, coupled with the first Langmuir adsorption model, are solved using the finite element method (FEM) with the Galerkin approach. A computer code has been developed to compute the numerical solution<sup>41</sup>. First, triangular elements are used to discretize the domain and the mesh is refined near the reaction surface and electrodes to improve the quality. All variables are then approximated by polynomials within each element. Subsequently, the concentrations of the target antigen,  $[A](x, y, t)$ , in the microchannel and the antigen-antibody complex,  $[AB](x, t)$ , on the sensitive surface were obtained by simultaneously solving the antigen transport and the binding reaction equations in a time-dependent regime. In this study, the target antigen is the SARS-CoV-2 virus, and the ligand is its corresponding antibody (b1 or h12)<sup>21</sup>. To compute the total concentration of the formed complexes (SARS-CoV-2-antibody), the local concentration was integrated over the entire length of the binding surface (Eq. 14) and the normalized surface concentration of

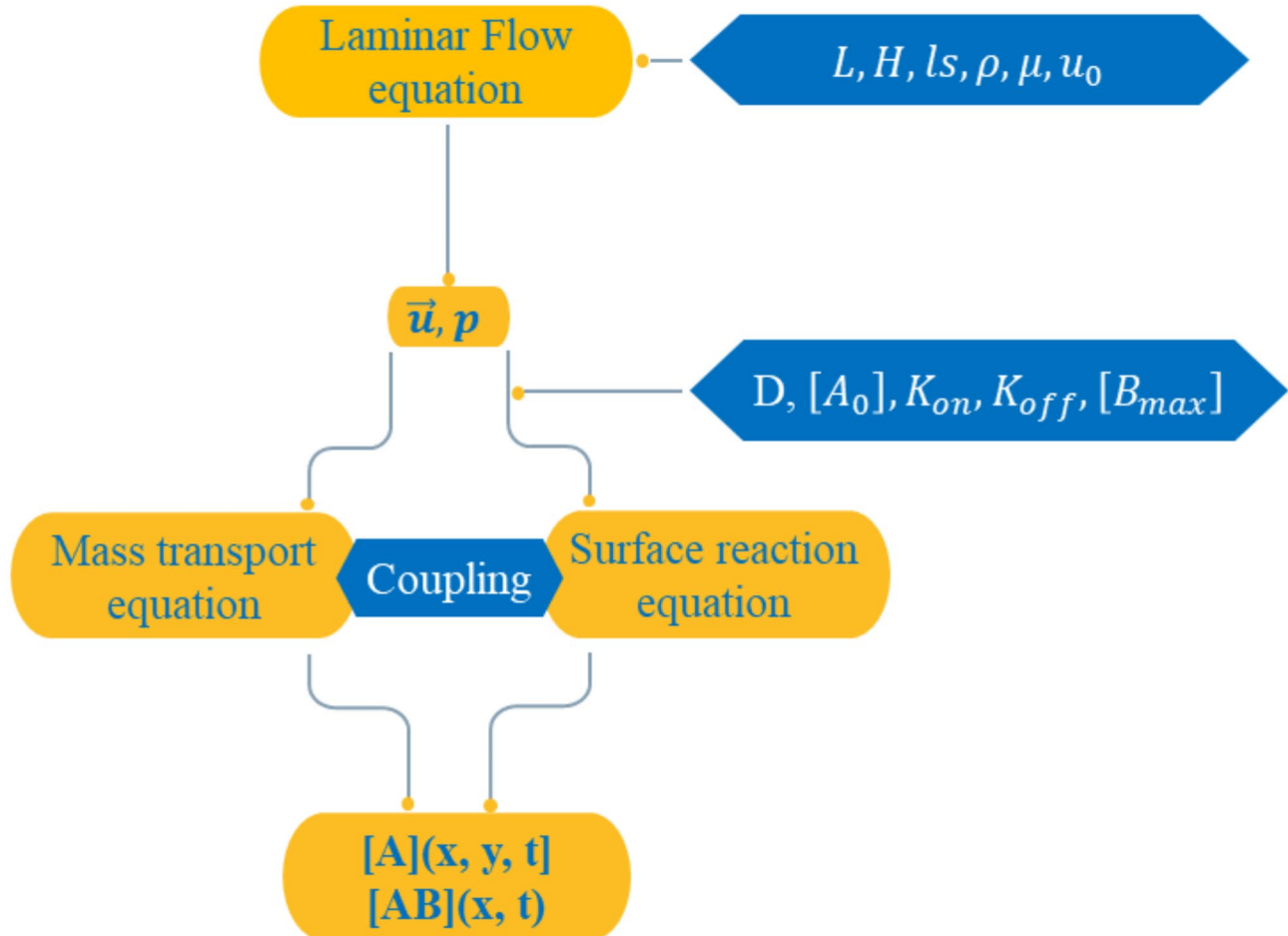


**Fig. 3.** Algorithm of numerical simulation protocols.

these complexes,  $[AB]$ , was then calculated by dividing the total concentration by the concentration of binding sites on the biosensor surface,  $[B_{max}]$ .

Grid independence was assessed through a mesh sensitivity analysis of the dimensionless velocity profile along the y-axis at dimensionless  $x = 2$  for several meshes (764, 1092, 1128 and 1549 elements) as shown in Fig. 4.

The error results show that the relative variation of successive values of  $u$  at each mesh point is calculated using the following expression:

$$Error_j = \left| \frac{u_{i+1} - u_i}{u_i} \right| \times 100$$

For other values of  $x$ , the fluctuating errors indicate more or less significant variations in  $u(i)$ . For example, for  $x = 0.0313$ , the error for Error1 and Error2 is about 1%, while Error3 has a much smaller error (0.54%) (Fig. 5). This indicates that the successive variations of  $u$  are larger for Error1 and Error2 and more stable for Error3. In summary, the error peaks correspond to abrupt changes in  $u$ , while the smaller errors indicate a more regular variation of  $u$ . In conclusion, since the error of mesh 2 compared to mesh 1 remains less than 5%, mesh 2 (composed of 1092 elements) is retained for this optimization study.

## Results and discussion

### Model validation

First, the numerical model was validated by comparing it with the experimental data of Berthier and Silberzan<sup>21</sup>, as shown in Fig. 6. The time-normalized surface concentration during the adsorption phase was calculated using the same experimental parameters within a microfluidic channel measuring 1 mm in height and 1 cm in width. The target antigens' concentration and their diffusion constant are  $2.5 \times 10^{-6}$  Mol/m<sup>3</sup> and  $7 \times 10^{-11}$  m<sup>2</sup>/s, respectively. The flow rate of the carrier fluid is  $10^{-6}$  m<sup>3</sup>/s. The density of binding sites, the association constant, and the dissociation constant are  $1.668 \times 10^{-8}$  Mol/m<sup>2</sup>, 75 m<sup>3</sup>/Mol·s and  $10^{-2}$  1/s, respectively.

The following coefficients, namely the Root Mean Square Error (RMSE) and the Mean Absolute Percentage Error (MAPE), are calculated to evaluate the performance of the model proposed in this study<sup>42,43</sup>.

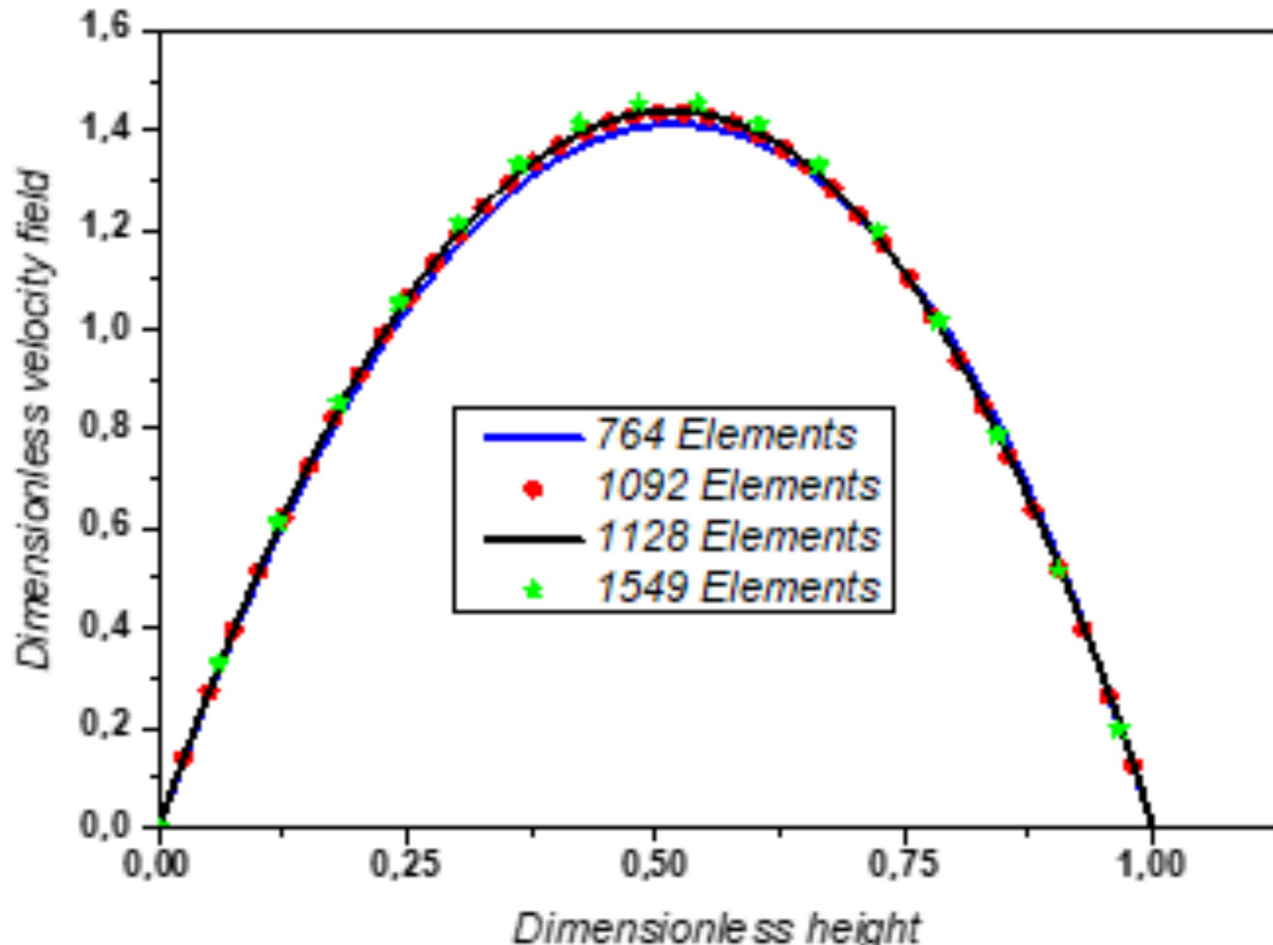


**Fig. 4.** Dimensionless velocity profile along the y-axis at dimensionless  $x = 2$  for different mesh grids.

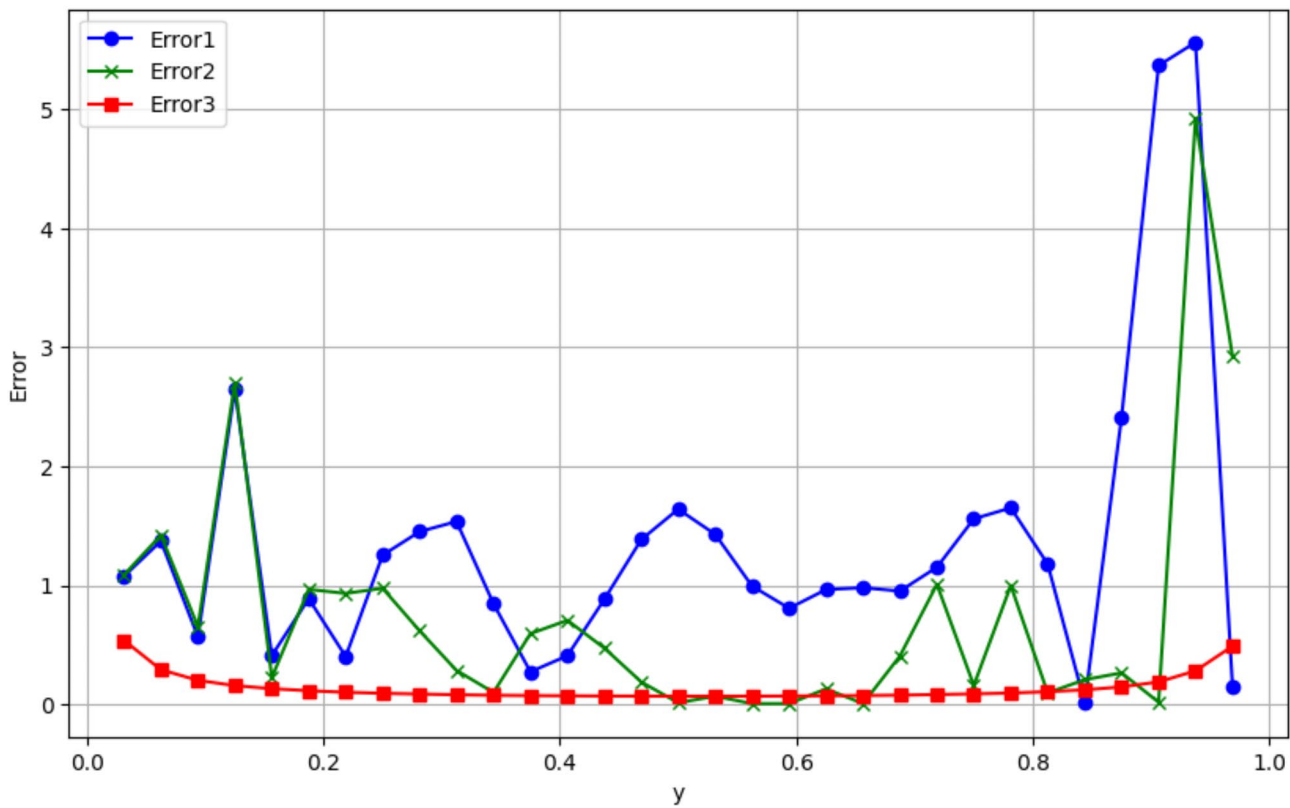


**Fig. 5.** Distribution of relative error along the y-axis for different meshes.

$$RMSE = \sqrt{\frac{1}{N} \sum_{i=1}^N (y_i - \hat{y}_i)^2} \quad (15)$$

$$MAPE = \frac{1}{N} \sum_{i=1}^N \left| \frac{y_i - \hat{y}_i}{y_i} \right| \times 100 \quad (16)$$

where  $y$  is the actual value obtained by the experimental data and  $\hat{y}$  is the predicted value using one of the model and  $N$  and  $N$  are numbers of observations.

The calculated Mean Absolute Error (MAE) of 0.0180 and Root Mean Square Error (RMSE) of 0.0298 indicate that the model's predictions are quite accurate. The small MAE suggests that, on average, the model's predictions deviate by only 0.0180 units from the experimental data, while the slightly higher RMSE reflects some larger deviations. Overall, the model demonstrates good performance in predicting the response with minimal error.

## 2D approximation for microfluidic biosensor analysis

The graph of Fig. 7 shows the evolution of the normalized concentration of the complex as a function of time for both the 2D and 3D models. The results show a slight underprediction bias with a mean error of -0.002476. The errors are consistent, as indicated by the low standard deviation of 0.006587112, and the maximum error is small at 0.00513, indicating good overall accuracy and stability.

This similarity shows that the 2D approximation faithfully reproduces the results of the 3D model, justifying its use for the study of the microfluidic biosensor while preferentially reducing the computational cost.

## Parameters and levels selection

To evaluate the influence of control parameters on SARS-CoV-2 binding kinetics, we performed numerical simulations using the geometric design of the microfluidic biosensor shown in Fig. 1. The simulation parameters employed in this study include the input volume concentration of the SARS-CoV-2 antigen ( $[A_0] = 10^{-7} \text{ Mol.m}^{-3}$ ), the antibody concentration on the sensitive surface ( $[B_{max}] = 3.3 \cdot 10^{-8} \text{ Mol.m}^{-2}$ ), and the equilibrium desorption constant ( $K_d = 10^{-6} \text{ Mol.m}^{-3}$ ), which align with values reported in the literature<sup>17–19,21,44</sup>. Consequently, the relative density of the analyte-ligand complex,  $\sigma$ , is determined to  $1.2 \cdot 10^{-4}$ . In this study, different controllable parameters were chosen for optimization to maximize the biosensor's efficiency. The Reynolds number (Re), Damkohler number (Da), Schmidt number (Sc), and the position of the

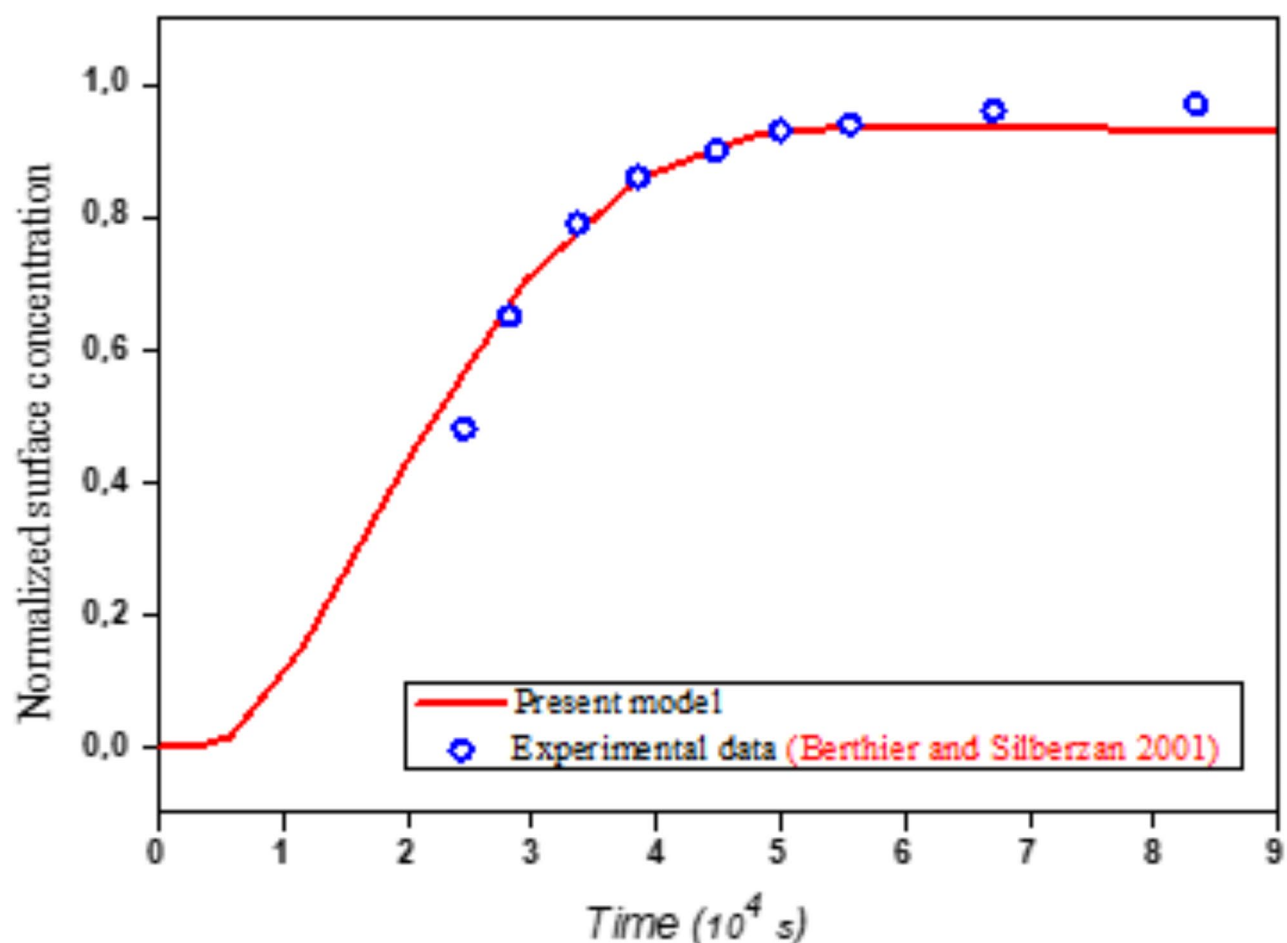


**Fig. 6.** Comparison of our model with the experimental data from Berthier and Silberzan<sup>21</sup>.

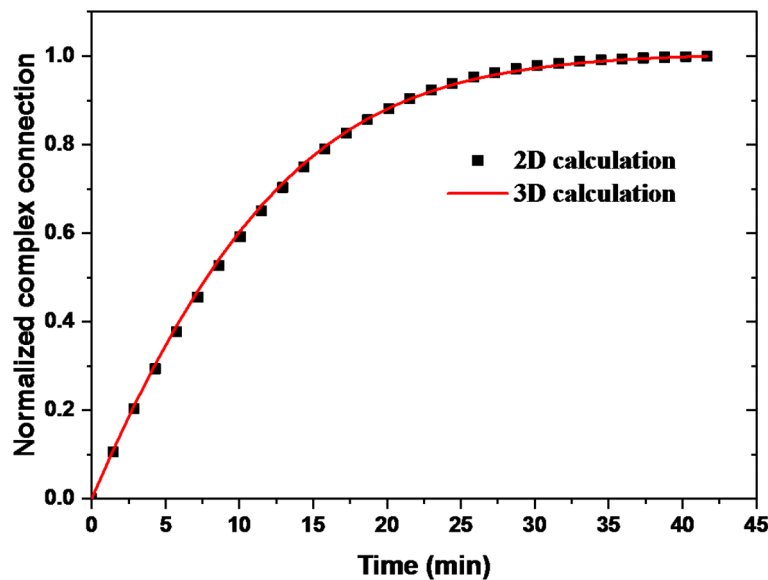


**Fig. 7.** Comparison between 3D and 2D calculation.

Symbol	Optimization parameter	Level 1	Level 2	Level 3
A	Reynolds number (Re)	$4.10^{-3}$	$2.10^{-2}$	$4.10^{-2}$
B	Damkohler number (Da)	5	500	1000
C	Schmidt number (Sc)	$10^4$	$5.10^4$	$10^5$
D	Reaction surface position (X)	1	2.5	4

**Table 1.** Selected optimization factors and respective levels.

Experiment tests	Factors levels			
	A	B	C	D
1	1	1	1	1
2	1	2	2	2
3	1	3	3	3
4	2	1	2	3
5	2	2	3	1
6	2	3	1	2
7	3	1	3	2
8	3	2	1	3
9	3	3	2	1

**Table 2.** The Taguchi  $L_9(3^4)$  orthogonal table.

reaction surface (X) are the four variables targeted for optimization using the Taguchi method, with the objective of achieving the shortest detection time.

#### Reynolds number

In microfluidic devices, flow velocities typically remain low, ranging from a few tenths of a millimeter per second. For water as the carrier fluid ( $\rho = 10^3 \text{ kg m}^{-3}$ ,  $\mu = 1.08 \times 10^{-3} \text{ Pa s}$ ), the Reynolds number varies between  $4.10^{-3}$  and  $4.10^{-2}$  for flow velocities ranging from  $10^{-4}$  to  $10^{-3} \text{ m s}^{-1}$ <sup>45,46</sup>.

#### Damkohler number

With the surface concentration of binding sites fixed ( $[B_{max}] = 3, 3 \times 10^{-8} \text{ mol m}^{-2}$ ) and the microchannel height ( $H = 40.10^{-6} \text{ m}$ ), the Damkohler number is influenced solely by the diffusion coefficient of the target antigen (D) and the adsorption antigen-antibody constant ( $K_{on}$ ). For SARS-CoV-2, with the diffusion coefficient ranging from  $10^{-11}$  to  $10^{-10} \text{ m}^2 \text{ s}^{-1}$  and the adsorption constant between  $10^2$  and  $10^4 \text{ m}^3/\text{Mol.s}$ , the Damkohler number can fluctuate between 1 and 1000<sup>10,47,48</sup>.

#### Schmidt number

Given that the Schmidt number ( $Sc = \frac{Pe}{Re}$ ) is inversely proportional to the antigen diffusion coefficient (D) for a given density and dynamic viscosity of the carrier fluid, it can vary between  $10^4$  and  $10^5$  for the same range of D variation indicated previously<sup>19</sup>.

#### Taguchi method optimization

The Taguchi method was employed in this numerical simulation to streamline the testing process for achieving the shortest detection time in the microfluidic biosensor. The selection of the Taguchi Design of Experiments methodology is justified by its systematic and efficient approach to optimizing process parameters. The Taguchi method allows for a reduction in the number of experiments required to determine optimal conditions, which is particularly useful in complex systems like microfluidic biosensors<sup>49</sup>.

Table 1 outlines the four factors influencing the detection system, each with three levels denoted as “1,” “2,” and “3,” representing the lowest, mid, and highest levels, respectively. Considering these factors (A, B, C, and D), conducting experiments for all possible combinations would require  $3^4 = 81$  trials. To minimize the number of experiments, the Taguchi method was applied using the orthogonal table  $L_9(3^4)$ , as presented in Table 2. This approach reduced the number of experiments to nine, involving four critical parameters at three levels each, without considering their interactions.

In each test, the factors are set at levels 1, 2, or 3. Figure 8 illustrates the average normalized dimensionless concentration of the antigen-antibody complex over dimensionless time for all experimental tests conducted according to Table 2.

In the Taguchi design of experiments, we manipulate noise factors to intentionally introduce variability. From the obtained results, we can identify optimal parameters that make the detection process robust against variations caused by these noise factors. A high signal-to-noise ratio (S/N) value indicates that the control factor parameters effectively limit the effects of the noise factors. The S/N ratio, calculated based on the “smaller is better” criteria for each test, is determined using Eq. (15)<sup>50</sup>, and the results are recorded in Table 3.

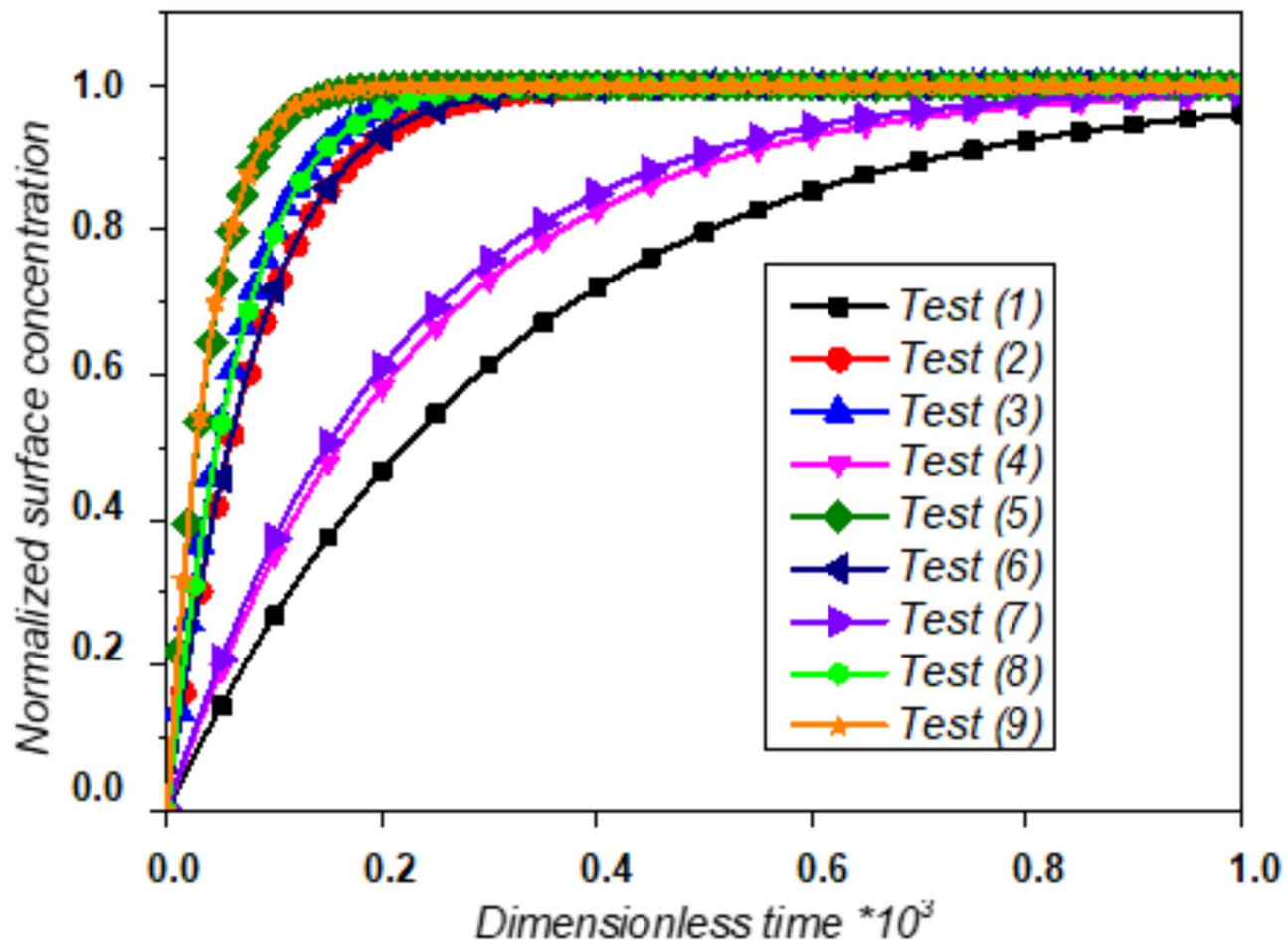


**Fig. 8.** Normalized complex concentration versus time for the nine Taguchi tests.

Experimental run	Designation	Dimensionless Response time ( $T_R$ )	S/N ratio for $T_R$
1	$A_1B_1C_1D_1$	930	-59,3697
2	$A_1B_2C_2D_2$	225	-47,0437
3	$A_1B_3C_3D_3$	175	-44,8608
4	$A_2B_1C_2D_3$	680	-56,6502
5	$A_2B_2C_3D_1$	105	-40,4238
6	$A_2B_3C_1D_2$	220	-46,8485
7	$A_3B_1C_3D_2$	630	-55,9868
8	$A_3B_2C_1D_3$	170	-44,6090
9	$A_3B_3C_2D_1$	100	-40,0000

**Table 3.** The Taguchi  $L_9(3^4)$  designation with four factors at three levels, detection time, and S/N ratio obtained from the corresponding runs.

$$S/N = -10\log \left( \frac{1}{n} \sum_{i=1}^n Y_i^2 \right) \quad (17)$$

Here,  $S$  represents the signal value,  $N$  is the noise value,  $n$  is the number of simulation tests, and  $y_i$  is the measured response value (detection time of the  $i^{\text{th}}$  simulation). A higher S/N value indicates better performance<sup>50</sup>, and the optimal level of each parameter is specified by a higher S/N values. Table 3 shows the numerical results for the biosensor's response time ( $T_R$ ) and its corresponding S/N ratio using the experimental layout.

To evaluate the impact of each key parameter, it is essential to calculate the mean values of the responses for each level. This involves summing the results associated with each level in the orthogonal table and dividing

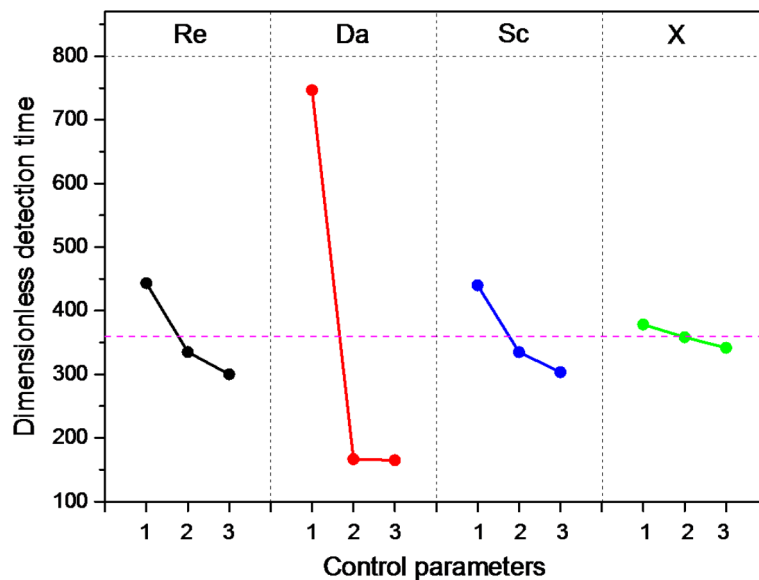


**Fig. 9.** Main effect plots of each key parameter on the detection time of the device.

Level	Re	Da	Sc	X
1	– 50,42	– 57,34	– 50,28	– 46,60
2	– 47,97	– 44,03	– 47,90	– 49,96
3	– 46,87	– 43,90	– 47,09	– 48,71
Delta = Max-Min	3,56	13,43	3,19	3,36
Rank	2	1	4	3

**Table 4.** Signal to noise ratios for each level.

by the number of tests for that level to obtain the appropriate averages. Figure 9 visually represents the average effects of the four factors considered in this study. The factor with the most substantial influence is identified by the difference values (Delta) between the maximum and minimum values of the three averages. The greater the difference, the more influential the control factor. In Fig. 9, the Damkohler number stands out as having the strongest influence.

The significance of each key parameter is further analyzed in Table 4 by subtracting the maximum S/N ratio from its minimum value across the three levels. Parameters with minimal differences in the S/N ratio play a smaller role in controlling the synthesis process<sup>37</sup>.

The Schmidt number (Sc) plays a key role in antigen diffusion and, consequently, on the detection time. Being defined as the ratio of momentum diffusivity to mass diffusivity ( $Sc = v/D$ ), a high Sc implies a lower antigen diffusivity, which can prolong the detection time. Conversely, a lower Sc favors diffusion and can thus improve the detection efficiency. In order to better answer this question, we will add an in-depth discussion supported by numerical results to illustrate the impact of Sc variation on antigen transport and detection performance. In particular, we will analyze the evolution of antigen concentration as a function of time for different Sc values, thus highlighting its effect on the sensor efficiency<sup>51</sup>.

Plotting the S/N ratio against each key parameters, as per the values in Table 4, reveals in Fig. 10 that, according to the Taguchi method, the lowest value of the biochip's response time is reached at the highest levels of the Reynolds number ( $4 \times 10^{-2}$ ), Damkohler number ( $10^3$ ), Schmidt number ( $10^5$ ), and the lowest level of the reaction surface position (1). Interestingly, the optimal combination ( $A_3B_3C_3D_1$ ) was not among the nine tests of the  $L_9$  orthogonal network, but Taguchi's method successfully identified it.

To justify the robustness of the optimization process with the Taguchi method and ensure the reliability of the S/N ratios and ANOVA results, we performed a new simulation of the biosensor's response time using the optimized parameters. This validation procedure yielded a dimensionless detection time value of 80 (~ 21 min), the lowest among those obtained in the original  $L_9$  experiments, thus confirming the effectiveness of the optimization approach. Under optimal conditions, the limit of detection (LOD) and the limit of quantification (LOQ) were calculated 2.197 pmol/L and 6.659 pmol/L respectively.

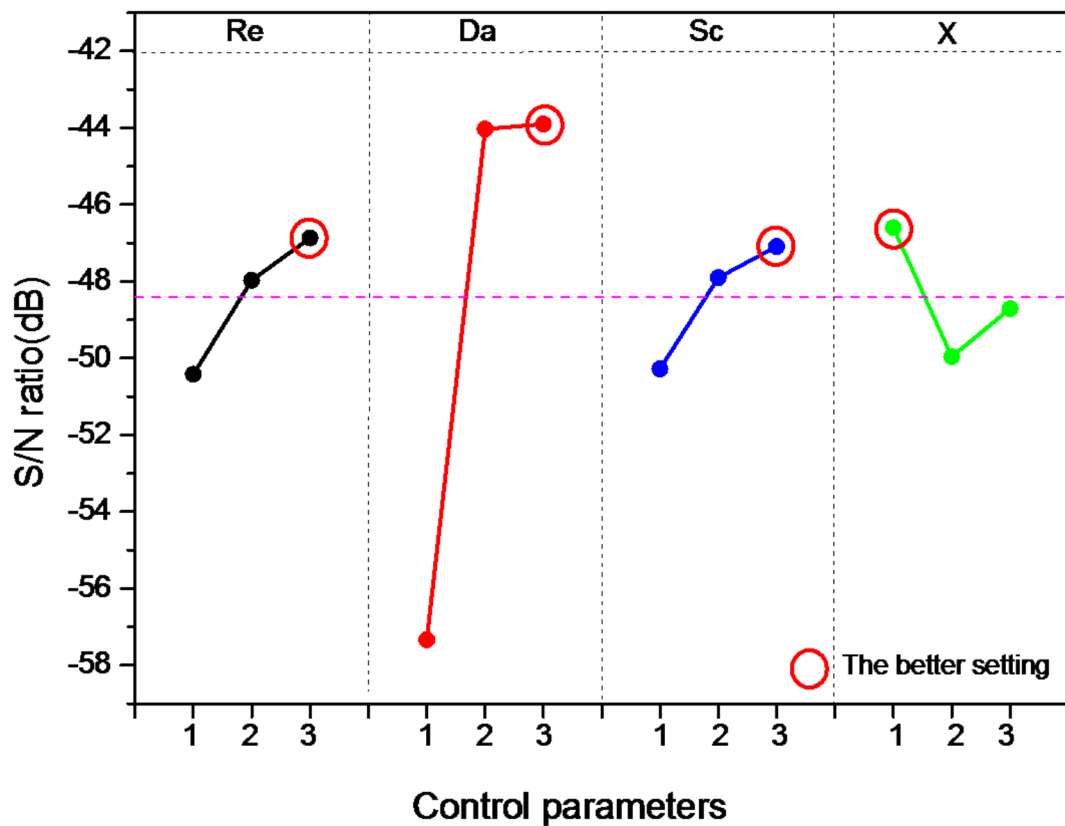


**Fig. 10.** S/N ratio for the four key parameters at different levels.

#### ANOVA analysis

Following the ANOVA scheme used for the  $L_9$  Taguchi method<sup>52</sup>, the percentage contribution of each key parameter to the detection time is determined in this work. The equations used in this analysis are as follows (Eqs. 16, 17, 18, 19, 20):

- The average of all response times ( $\bar{T}_R$ ) is calculated as:

$$\bar{T}_R = \frac{1}{9} \sum_{i=1}^9 T_{R_i} \quad (18)$$

- The total sum of squares ( $SS_{Total}$ ) is determined by:

$$SS_{Total} = \sum_{i=1}^9 (T_{R_i} - \bar{T}_R)^2 \quad (19)$$

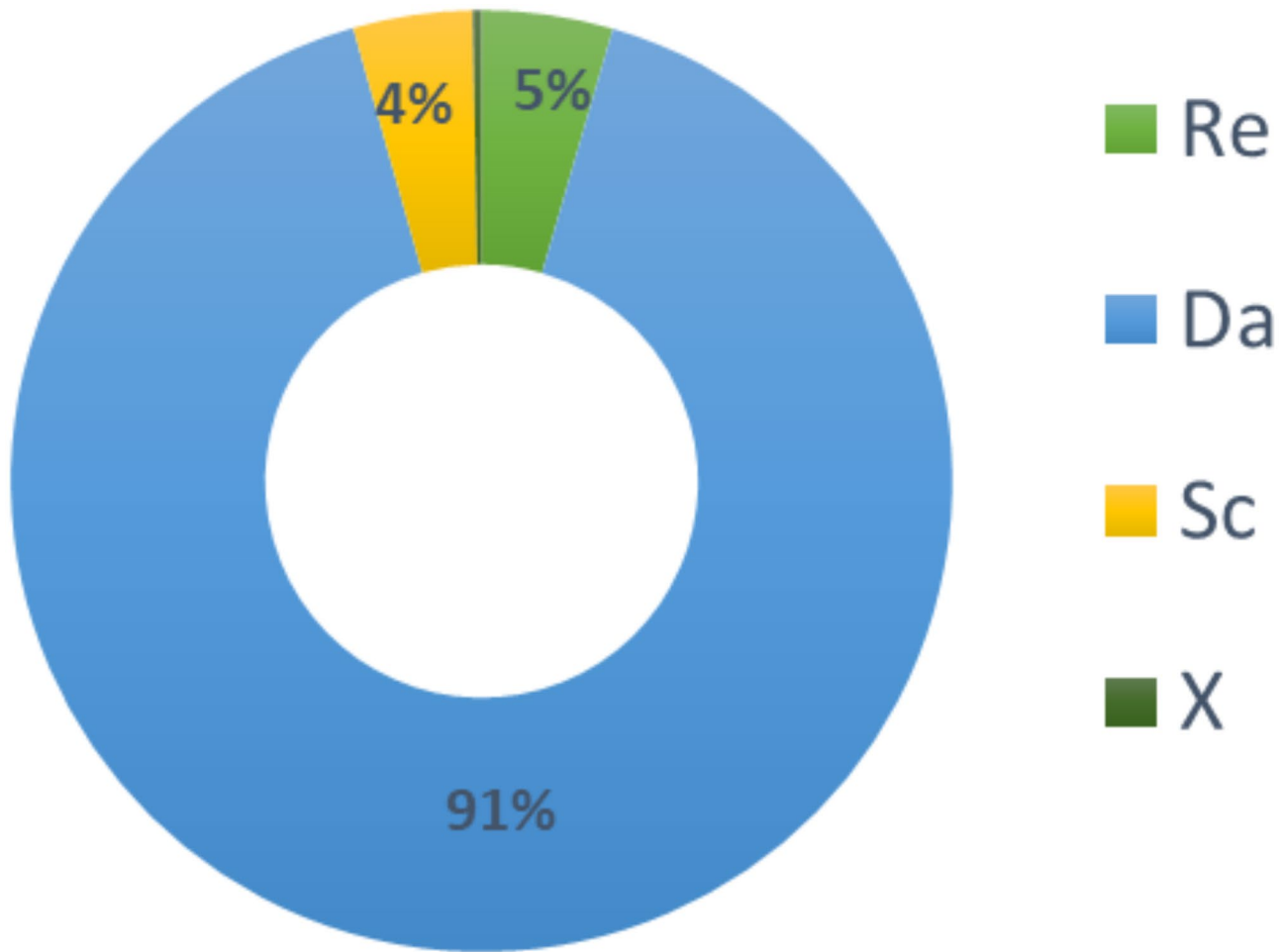
- The sum of squares for Reynolds number ( $SS_{Re}$ ), Damkohler number ( $SS_{Da}$ ), Schmidt number ( $SS_{Sc}$ ) and reaction surface position ( $SS_X$ ) are given by:

$$SS_{Re} = 3 \sum_{i=1}^3 (T_{R_{Rei}} - \bar{T}_R)^2, \quad SS_{Da} = 3 \sum_{i=1}^3 (T_{R_{Dai}} - \bar{T}_R)^2, \quad SS_{Sc} = 3 \sum_{i=1}^3 (T_{R_{Sci}} - \bar{T}_R)^2 \quad \text{and} \\ SS_X = 3 \sum_{i=1}^3 (T_{R_{Xi}} - \bar{T}_R)^2 \quad (20)$$

where  $T_{R_{Xi}}$  is the  $i$ -th average response time of the corresponding parameter  $x$  (Re, Da, Sc, X) in the Taguchi design.

- the mean squares for each parameter are:

Source	DF	SS	MS	% Contribution
Re	2	33,506	16,753	4.5
Da	2	674,739	337,369	91.1
Sc	2	30,706	15,353	4.1
X	2	2022	1011	0.3
Residual error	0	0	0	0
Total	8	740,972		100

**Table 5.** ANOVA results on the detection time response.**Fig. 11.** Contributions of key parameters to biosensor detection time.

$$MS_{Re} = \frac{SS_{Re}}{DF_{Re}}, \quad MS_{Da} = \frac{SS_{Da}}{DF_{Da}}, \quad MS_{Sc} = \frac{SS_{Sc}}{DF_{Sc}} \quad \text{and} \quad MS_X = \frac{SS_X}{DF_X} \quad (21)$$

where DF is the degree of freedom (2 = number of level – 1).

- The contribution percentages for each parameter are:

$$\begin{aligned} \% \text{ contribution Re} &= \frac{SS_{Re}}{SS_{Total}}, \quad \% \text{ contribution Da} = \frac{SS_{Da}}{SS_{Total}}, \quad \% \text{ contribution Sc} = \frac{SS_{Sc}}{SS_{Total}} \quad \text{and} \\ \% \text{ contribution X} &= \frac{SS_X}{SS_{Total}} \end{aligned} \quad (22)$$

The obtained results are presented in Table 5; Fig. 11. Among the key parameters, the Damkohler number (Da) has the highest contribution (91.1%) to reducing the response time of the device, while the reaction surface position (X) has the lowest contribution (0.3%).

Figure 12a shows the normalized complex concentration for the optimal test using the optimized parameters, while Fig. 12b,c illustrate the antigen diffusion boundary layers near the reaction surface at dimensionless adsorption times of 50 and 150, respectively. Notably, at  $t=150$  (where  $t$  is the dimensionless saturation time), the diffusion boundary layer thickness is remarkably thin, indicating efficient mass transport for the analyte-ligand bond in the optimal test. This improvement in mass transport efficiency contributes to the enhanced performance of the biosensor.

#### ANN-MLP predictions

The Multi-Layer Perceptron Artificial Neural Network (ANN-MLP) is a type of ANN distinguished by its interconnected layers, including input, hidden, and output layers, widely applied in machine learning tasks like classification and pattern recognition<sup>53,54</sup>. Learning in ANN-MLP occurs through weight and bias adjustments during training<sup>55</sup>. An exhaustive investigation of 81 simulation data points derived from the Full L<sub>81</sub>(3<sup>4</sup>) design experiment was utilized to train various networks with different quantities of hidden layer neurons. The training process employed back-propagation with gradient descent, dividing the dataset into training (70%), testing (15%), and validation (15%) subsets.

The following coefficients are calculated to control the performance of the proposed models in this study<sup>42,43</sup>. The first coefficient is the value of the root mean square error.

$$RMSE = \sqrt{\frac{1}{N} \sum_{i=1}^N (y_i - \hat{y}_i)^2} \quad (23)$$

where  $N$  and are numbers of observations.

We can also use the coefficient of determination  $R^2$  to evaluate the performance of the prediction. This coefficient is given by<sup>32</sup>:

$$R^2 = 1 - \frac{\sum_{i=1}^N (y_i - \hat{y}_i)^2}{\sum_{i=1}^N (y_i - \bar{y})^2} \quad (24)$$

where  $\bar{y}$  is average value of  $y$ .

The numerator in the above equation corresponds to the sum of squares of residuals whereas the denominator is related to the variance of the data. The best prediction is obtained when the coefficient of determination  $R^2$  is close to one.

When the number  $k$  of input variables of the model increases, the coefficient of determination  $R^2$  automatically increases. To correct this bias, an adjusted coefficient is proposed. It is defined by<sup>56</sup>:

$$R_{Adj}^2 = 1 - (1 - R^2) \frac{N - 1}{N - k - 1} \quad (25)$$

Figure 13 assesses the ANN-MLP model's ability to predict the biosensor's detection time. Subplot (a) compares simulated and predicted values, demonstrating the alignment between model predictions and actual data.

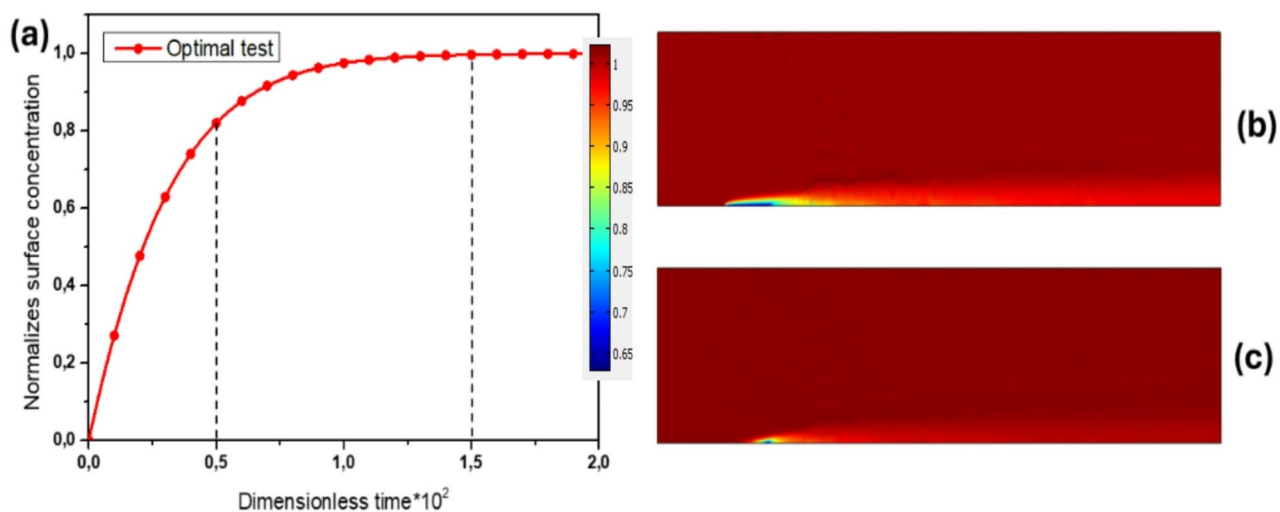


**Fig. 12.** (a) Normalized surface concentration for the optimal test. (b) and (c) diffusion boundary layers during the adsorption phase at two dimensionless times,  $T_R = 50$  and  $T_R = 150$ , respectively.

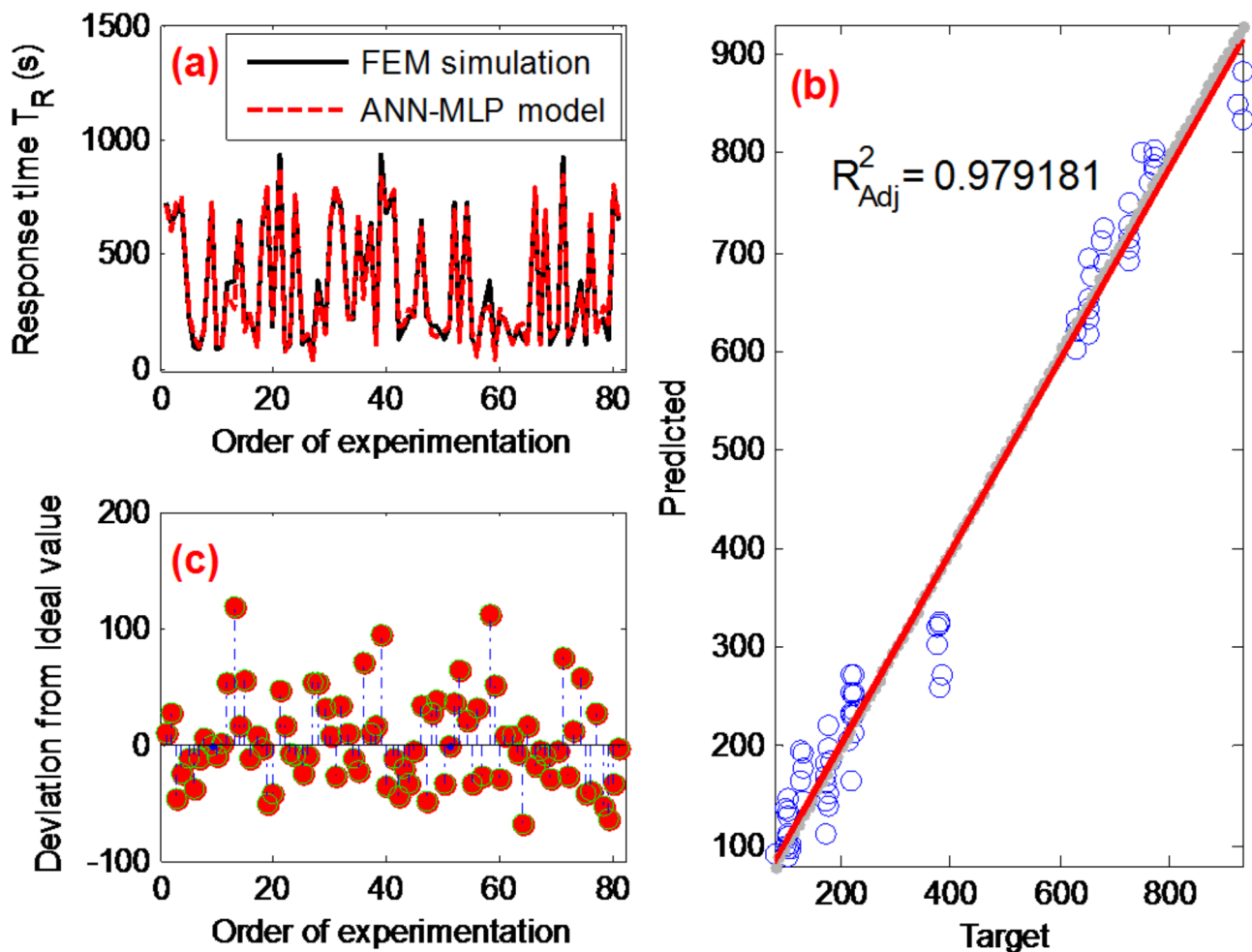


**Fig. 13.** (a) Comparison of observed response time values using the ANN-MLP model; (b) statistical analysis fit of the ANN-MLP model; (c) deviation analysis of the ANN-MLP model predictions from actual response time values.

Subplot (b) presents a statistical analysis fit, evaluating the degree of fit between predicted and actual values. In subplot (c), the deviation of predicted values from actual values is examined, aiding in understanding predictive errors and discrepancies. With an achieved adjusted coefficient of determination ( $R^2_{Adj}$ ) of 0.97 and a root mean square error (RMSE) of 42.12, the model demonstrates effective predictive capability.

#### ANN-PSO predictions

The incorporation of the Particle Swarm Optimization (PSO) algorithm into a traditional Artificial Neural Network (ANN) presents a promising approach. It optimizes the connection weights within the ANN, aiming to identify the optimal values that yield the best results. The PSO algorithm begins by generating a population of particles, each representing a potential solution set to be employed within the neural network<sup>57</sup>. Evaluating the fitness of each particle involves considering local and global information, and this information is retained within each particle. PSO uses this data to update particle velocities and efficiently explore the solution space.

The choice of the ANN-PSO algorithm is based on its ability to efficiently deal with complex and non-linear optimization problems (like our case). The combination of ANN for predictive modeling and PSO for parameter optimization improves the prediction of biosensor performance. This method showed superior results in terms of prediction accuracy and computational efficiency compared to other tested optimization algorithms<sup>31,32</sup>.

Configured with a swarm size of 150, a cognitive coefficient ( $C_1$ ) of 1.5, a social coefficient ( $C_2$ ) of 2, and an inertia weight ( $W$ ) of 0.9, the ANN-PSO model delivers highly accurate predictive results, evidenced by an outstanding adjusted regression coefficient of 0.98 (as illustrated in Fig. 14). The performance metrics, including  $RMSE = 33.2$ , and  $R^2 = 0.99$ , consistently demonstrate the superiority of the PSO-ANN model in capturing and predicting complex patterns in the Full  $L_{81}(3^4)$  given data.

#### Conclusion

This study presents a numerical optimization of a microfluidic chip designed for rapid COVID-19 bioassays. By thoroughly analyzing the kinetics of the SARS-CoV-2 binding reaction, we identified four key control

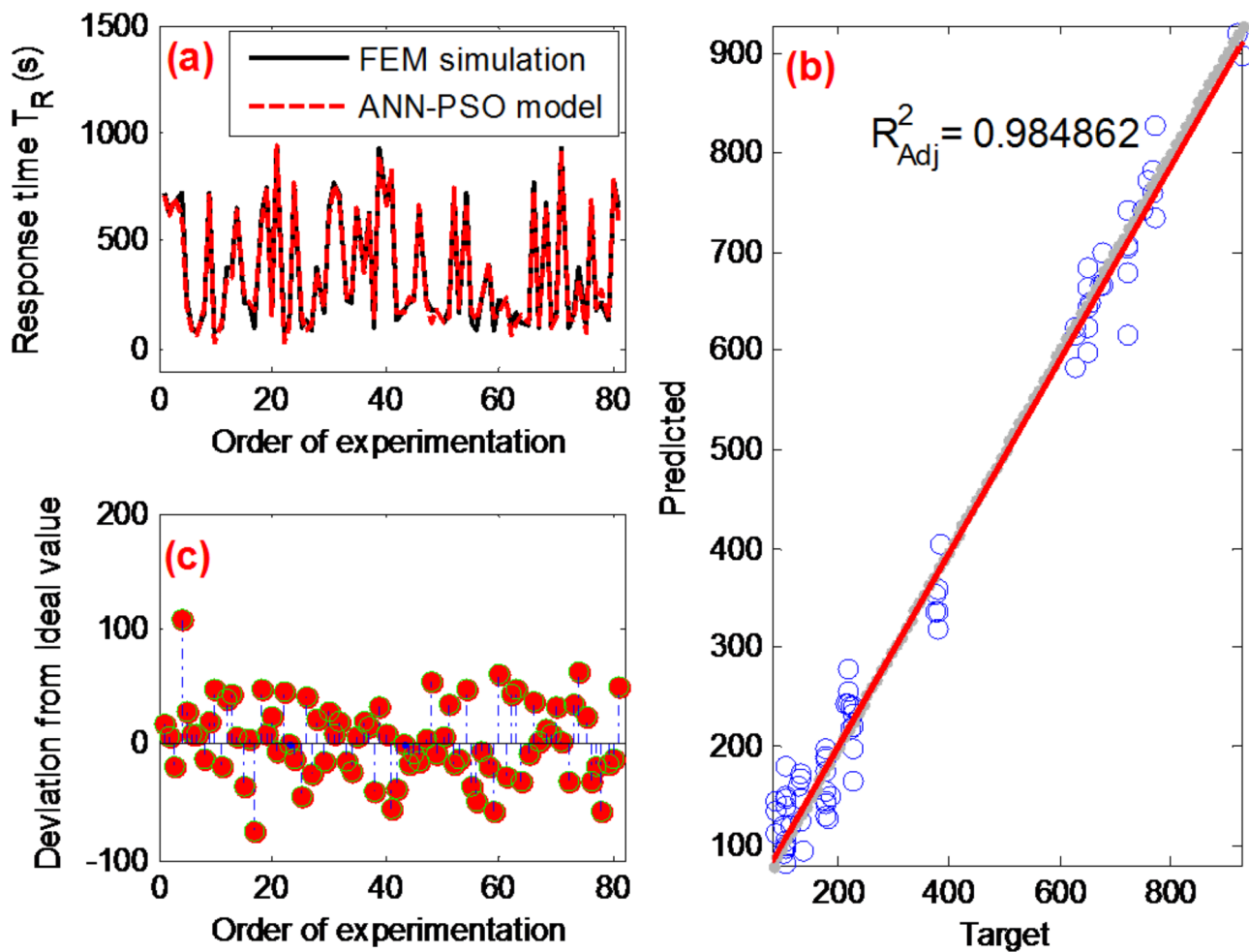


**Fig. 14.** (a) Comparison of observed response time values using ANN-PSO model; (b) statistical analysis fit of the ANN-PSO model; (c) deviation analysis of ANN-PSO model predictions from actual response time values.

parameters: the Reynolds number, Damkohler number, Schmidt number, and the position of the reaction surface. To optimize these key parameters, we used the Taguchi method in conjunction with ANOVA, reducing the number of required simulations from 81 to just 9 using the  $L_9(3^4)$  orthogonal array. These approaches allowed us to efficiently explore the optimal combination of key parameters and their effects on biosensor performance. The optimal combination corresponds to a Reynolds number (Re) of 0.04 (level 3), a Damkohler number (Da) of 1000 (level 3), a Schmidt number (Sc) of 100,000 (level 3), and a dimensionless reaction surface position (X) of 1 (level 1).

Using the optimized values, the biosensor detection time was significantly reduced to 21 min, demonstrating the potential for rapid COVID-19 detection. Furthermore, the integration of Particle Swarm Optimization (PSO) with an Artificial Neural Network (ANN-PSO) significantly improved the predictive accuracy and robustness of our approach compared to the conventional ANN-MLP model.

This study underscores the effectiveness of combining the Taguchi method, ANOVA, and ANN-PSO for optimizing microfluidic biosensors, paving the way for rapid, efficient, and accurate COVID-19 detection. The proposed methodology not only offers significant improvements in biosensor performance but also holds promise for broader applications in the field of bioassays in general.

### Data availability

The data that support the findings of this study are available from the corresponding author upon reasonable request.

Received: 10 September 2024; Accepted: 10 April 2025

Published online: 23 April 2025

### References

- Choi, J. R. Development of point-of-care biosensors for COVID-19. *Front. Chem.* **8**, 517 (2020).

2. Orooji, Y. et al. An overview on SARS-CoV-2 (COVID-19) and other human coronaviruses and their detection capability via amplification assay, chemical sensing, biosensing, Immunosensing, and clinical assays. *Nano-micro Lett.* **13**, 1–30 (2021).
3. Vemula, S. V. et al. Current approaches for diagnosis of influenza virus infections in humans. *Viruses* **8**, 96 (2016).
4. Pachucki, C. T., Khurshid, M. A. & Nawrocki, J. Utility of reverse transcriptase PCR for rapid diagnosis of influenza a virus infection and detection of amantadine-resistant influenza a virus isolates. *J. Clin. Microbiol.* **42**, 2796–2798 (2004).
5. Madadelahi, M., Agarwal, R., Martinez-Chapa, S. O. & Madou, M. J. A roadmap to high-speed polymerase chain reaction (PCR): COVID-19 as a technology accelerator. *Biosens. Bioelectron.* **246**, 115830 (2024).
6. Sheridan, C. Fast, portable tests come online to curb coronavirus pandemic. *Nat. Biotechnol.* **38**, 515–518 (2020).
7. Zhifeng, J., Feng, A. & Li, T. Consistency analysis of COVID-19 nucleic acid tests and the changes of lung CT. *J. Clin. Virol.* **127**, 104359 (2020).
8. Sohrabi, H., Majidi, M. R., Asadpour-Zeynali, K., Khataee, A. & Mokhtarzadeh, A. Self-assembled monolayer-assisted label-free electrochemical genosensor for specific point-of-care determination of haemophilus influenzae. *Microchim. Acta* **190**, 112 (2023).
9. Tang, R. et al. A fully disposable and integrated paper-based device for nucleic acid extraction, amplification and detection. *Lab. Chip.* **17**, 1270–1279 (2017).
10. Sigurdson, M., Wang, D. & Meinhart, C. D. Electrothermal stirring for heterogeneous immunoassays. *Lab. Chip.* **5**, 1366–1373 (2005).
11. Morozov, V. N., Groves, S., Turell, M. J. & Bailey, C. Three minutes-long electrophoretically assisted zeptomolar microfluidic immunoassay with magnetic-beads detection. *J. Am. Chem. Soc.* **129**, 12628–12629 (2007).
12. Sackmann, E. K., Fulton, A. L. & Beebe, D. J. The present and future role of microfluidics in biomedical research. *Nature* **507**, 181–189 (2014).
13. Gervais, L., De Rooij, N. & Delamarche, E. Microfluidic chips for point-of-care immunodiagnostics. *Adv. Mater.* **23**, H151–H76 (2011).
14. Lynn Jr, N. S. et al. Biosensing enhancement using passive mixing structures for microarray-based sensors. *Biosens. Bioelectron.* **54**, 506–514 (2014).
15. Abedini-Nassab, R., Pouryousef Miandoab, M. & Şaşmaz, M. Microfluidic synthesis, control, and sensing of magnetic nanoparticles: A review. *Micromachines* **12**, 768 (2021).
16. Lee, G. U., Metzger, S., Natesan, M., Yanavich, C. & Dufrêne, Y. F. Implementation of force differentiation in the immunoassay. *Anal. Biochem.* **287**, 261–271 (2000).
17. Kaziz, S., Ben Mariem, I., Echouchene, F., Gazzah, M. H. & Belmabrouk, H. Design parameters optimization of an electrothermal flow biosensor for the SARS-CoV-2 S protein immunoassay. *Indian J. Phys.* **96**, 4091–4101 (2022).
18. Kaziz, S., Saad, Y., Bouzid, M., Selmi, M. & Belmabrouk, H. Enhancement of COVID-19 detection time by means of electrothermal force. *Microfluid. Nanofluid.* **25**, 1–12 (2021).
19. Kaziz, S., Saad, Y., Gazzah, M. H. & Belmabrouk, H. 3D simulation of microfluidic biosensor for SARS-CoV-2 S protein binding kinetics using new reaction surface design. *Eur. Phys. J. Plus.* **137**, 241 (2022).
20. Echouchene, F., Al-Shahrani, T. & Belmabrouk, H. Analysis of temperature-Jump boundary conditions on heat transfer for heterogeneous microfluidic immunoassays. *Sensors* **21**, 3502 (2021).
21. Shahbazi, F., Jabbari, M., Esfahani, M. N. & Keshmire, A. A computational simulation platform for designing real-time monitoring systems with application to COVID-19. *Biosens. Bioelectron.* **171**, 112716 (2021).
22. Maleki, F., Rashidi, M. R., Razmi, H. & Ghorbani, M. Label-free electrochemical immunosensor for detection of insulin-like growth factor-1 (IGF-1) using a specific monoclonal receptor on electrospun Zein-based nanofibers/rGO-modified electrode. *Talanta* **265**, 124844 (2023).
23. Sohrabi, H. et al. A PCR-free genosensing platform for detection of Shigella dysenteriae in human plasma samples by porous and honeycomb-like biochar decorated with ultrathin flower-like MoS<sub>2</sub> nanosheets incorporated with Au nanoparticles. *Chemosphere* **288**, 132531 (2022).
24. Sohrabi, H., Majidi, M. R., Asadpour-Zeynali, K., Khataee, A. & Mokhtarzadeh, A. Bimetallic Fe/Mn MOFs/M $\beta$ CD/AuNPs stabilized on MWCNTs for developing a label-free DNA-based genosensing bio-assay applied in the determination of *Salmonella typhimurium* in milk samples. *Chemosphere* **287**, 132373 (2022).
25. Sohrabi, H. et al. Emerging electrochemical sensing and biosensing approaches for detection of fumonisins in food samples. *Crit. Rev. Food Sci. Nutr.* **62**, 8761–8776 (2022).
26. Sohrabi, H. et al. Electrochemical-based sensing platforms for detection of glucose and H<sub>2</sub>O<sub>2</sub> by porous metal-organic frameworks: a review of status and prospects. *Biosensors* **13**, 347 (2023).
27. Daneshvar, N., Khataee, A., Rasoulifard, M. & Pourhassan, M. Biodegradation of dye solution containing malachite green: optimization of effective parameters using Taguchi method. *J. Hazard. Mater.* **143**, 214–219 (2007).
28. Ng, E. Y. & Ng, W. K. Parametric study of the biopotential equation for breast tumour identification using ANOVA and Taguchi method. *Med. Biol. Eng. Comput.* **44**, 131–139 (2006).
29. Romero-Villafranca, R., Zúñica, L. & Romero-Zúñica, R. Ds-optimal experimental plans for robust parameter design. *J. Stat. Plann. Inference.* **137**, 1488–1495 (2007).
30. Kaziz, S., Jemmalí, A. & Echouchene, F. Optimization of annular microfluidic biosensor enhanced by active and passive effects using Taguchi's method coupled with multi-layer perceptron neural networks (MLP-NN) models. *Microfluid. Nanofluid.* **27**, 60 (2023).
31. Jemmalí, A., Kaziz, S., Echouchene, F. & Gazzah, M. H. Optimization of Lab-on-a CD by experimental design and machine learning models for microfluidic biosensor application. *IEEE Sens. J.* (2024).
32. Kaziz, S., Echouchene, F. & Gazzah, M. H. Optimizing PCF-SPR sensor design through Taguchi approach, machine learning, and genetic algorithms. *Sci. Rep.* **14**, 7837 (2024).
33. Fountas, N. A., Benhadj-Djilali, R., Stergiou, C. I. & Vaxevanidis, N. M. An integrated framework for optimizing sculptured surface CNC tool paths based on direct software object evaluation and viral intelligence. *J. Intell. Manuf.* **30**, 1581–1599 (2019).
34. Fountas, N. A., Kanarachos, S. & Stergiou, C. I. Contrast-based fruit fly algorithm for optimizing conventional and nonconventional machining processes. *Int. J. Adv. Manuf. Technol.* **109**, 2901–2914 (2020).
35. Fountas, N. A., Kechagias, J. D. & Vaxevanidis, N. M. Optimization of selective laser sintering/melting operations by using a virus-evolutionary genetic algorithm. *Machines* **11**, 95 (2023).
36. Janmanee, P. & Muttamara, A. Optimization of electrical discharge machining of composite 90WC-10Co base on Taguchi approach. *Eur. J. Sci. Res.* **64**, 426–436 (2011).
37. Naresh, C., Pant, K., Bose, P. & Rao, C. *Optimization of Process Parameters on Performance Measures of Wire Electrical Discharge Machining on Niobium C-103 Using Taguchi Method, Recent Advances in Material Sciences: Select Proceedings of ICLIE2019* 409–423 (2018).
38. Zimmermann, M., Delamarche, E., Wolf, M. & Hunziker, P. Modeling and optimization of high-sensitivity, low-volume microfluidic-based surface immunoassays. *Biomed. Microdevices.* **7**, 99–110 (2005).
39. Wu, Y. et al. Enhancement of binding kinetics on affinity substrates using asymmetric electroosmotic flow on a sinusoidal bipolar electrode. *Micromachines* **13**, 207 (2022).
40. Baccouch, M. *Finite Element Methods and their Applications* (BoD—Books on Demand, 2021).
41. Selmi, M., Gazzah, M. H. & Belmabrouk, H. Optimization of microfluidic biosensor efficiency by means of fluid flow engineering. *Sci. Rep.* **7**, 1–11 (2017).

42. Amid, S., Mesri, T. & Gundoshmian Prediction of output energies for broiler production using linear regression, ANN (MLP, RBF), and ANFIS models. *Environ. Prog. Sustain. Energy.* **36**, 577–585 (2017).
43. Tayyebi, S., Hajjar, Z. & Soltanali, S. A novel modified training of radial basis network: prediction of conversion and selectivity in 1-hexene dimerization process. *Chemometr. Intell. Lab. Syst.* **190**, 1–9 (2019).
44. Kim, H. Y. et al. Development of a SARS-CoV-2-specific biosensor for antigen detection using scFv-Fc fusion proteins. *Biosens. Bioelectron.* **175**, 112868 (2021).
45. Mitra, S. K. & Chakraborty, S. *Microfluidics and Nanofluidics Handbook: Chemistry, Physics, and Life Science Principles* (CRC, 2011).
46. Kaziz, S., Ben Mariem, I., Echouchene, F., Belkhiria, M. & Belmabrouk, H. Taguchi optimization of integrated flow microfluidic biosensor for COVID-19 detection. *Eur. Phys. J. Plus.* **137**, 1235 (2022).
47. Ben Mariem, I., Kaziz, S., Belkhiria, M., Echouchene, F. & Belmabrouk, H. Numerical optimization of microfluidic biosensor detection time for the SARS-CoV-2 using the Taguchi method. *Indian J. Phys.* **97**, 2621–2628 (2023).
48. Chevalier, S., Tourville, J. N., Sommier, A. & Pradère, C. Infrared thermospectroscopic imaging of heat and mass transfers in laminar microfluidic reactive flows. *Chem. Eng. J. Adv.* **8**, 100166 (2021).
49. Ghabi, W. et al. Taguchi method and neural network for efficient  $\beta$ -ketoenamine synthesis in deionized water. *Can. J. Chem. Eng.* (2024).
50. Sayed, M. A., Dawood, O. M., Elsayed, A. H. & Daoush, W. R. Application of Taguchi method in optimization of process parameters of ODS tungsten heavy alloys. *Adv. Mater. Res.* **6**, 079 (2017).
51. Kaziz, S., Ben Romdhane, I., Echouchene, F. & Gazzah, M. H. Numerical simulation and optimization of AC electrothermal microfluidic biosensor for COVID-19 detection through Taguchi method and artificial network. *Eur. Phys. J. Plus.* **138**, 96 (2023).
52. Lakshminarayanan, A. & Balasubramanian, V. Process parameters optimization for friction stir welding of RDE-40 aluminium alloy using Taguchi technique. *Trans. Nonferrous Met. Soc. China.* **18**, 548–554 (2008).
53. Landolsi, K., Echouchene, F., Bajahzar, A., Belmabrouk, H. & Msaddek, M. Multiple linear regression and artificial neural networks for highly selective cationic  $\beta$ -diimine-methallyl nickel(II) catalyst for styrene dimerization reaction to 1,3-diphenyl-1-butene. *Appl. Organomet. Chem.* **37**, e7165 (2023).
54. Belkhiria, M., Jallouli, H., Bajahzar, A., Echouchene, F. & Belmabrouk, H. Optimization of electrothermal response of GAAFET using Taguchi's approach and an artificial neural network. *Case Stud. Therm. Eng.* **54**, 104047 (2024).
55. Massaoudi, A. et al. Machine learning models for modeling the biosorption of Fe (III) ions by activated carbon from Olive stone. *Neural Comput. Appl.* 1–16 (2024).
56. Massaoudi, A. et al. Modeling of the biosorption of Fe(III) ions by olive-stone activated carbon. *Appl. Organomet. Chem.* e7384.
57. Massaoudi, A. et al. Modeling of the biosorption of Fe(III) ions by olive-stone activated carbon. *Appl. Organomet. Chem.* e7384 (2024).

## Author contributions

S. K. : Conceptualization, Resources, Formal analysis, Writing-original draft. F. E. : Resources, Software, data curation, methodology, Writing-review & editing, Investigation. M.H.G. :Supervision, methodology, Project administration. All authors reviewed the manuscript.

## Declarations

### Competing interests

The authors declare no competing interests.

### Additional information

**Correspondence** and requests for materials should be addressed to M.H.G.

**Reprints and permissions information** is available at [www.nature.com/reprints](http://www.nature.com/reprints).

**Publisher's note** Springer Nature remains neutral with regard to jurisdictional claims in published maps and institutional affiliations.

**Open Access** This article is licensed under a Creative Commons Attribution 4.0 International License, which permits use, sharing, adaptation, distribution and reproduction in any medium or format, as long as you give appropriate credit to the original author(s) and the source, provide a link to the Creative Commons licence, and indicate if changes were made. The images or other third party material in this article are included in the article's Creative Commons licence, unless indicated otherwise in a credit line to the material. If material is not included in the article's Creative Commons licence and your intended use is not permitted by statutory regulation or exceeds the permitted use, you will need to obtain permission directly from the copyright holder. To view a copy of this licence, visit <http://creativecommons.org/licenses/by/4.0/>.

© The Author(s) 2025